Materials & Design 231 (2023) 112018

Contents lists available at ScienceDirect

Materials & Design

journal homepage: www.elsevier.com/locate/matdes

Novel femur-like multimodal ultrahigh strength structure with superb freedom based on the improvement strategy of curvature fabricated by additive manufacturing

Ruiyao Liu [a], Guofeng Yao [a], Zezhou Xu [b,*], Yuting Liu [b], Zhenglei Yu [b,*], Liang ping [b], Zhihui Zhang [b], Chunyang Han [c], Yunting Guo [b]

[a] Department of Mechanics, School of Mechanical and Aerospace Engineering, Jilin University, Changchun 130022, China
[b] Key Lab of Bionic Engineering, Ministry of Education, Jilin University, Changchun 130022, China
[c] Changchun Institute of Optics, Fine Mechanics and Physics, Chinese Academy of Sciences, Changchun 130022, China

HIGHLIGHTS

- The high curvature surface factor improves structural fracture behavior.
- The microstructure-properties relationship of 3D-printed Nylon is explained.
- Euler theory states mechanical properties are positive correlation with relative density.
- Explain how radial gradient variation enhances structural carrying capacity.

GRAPHICAL ABSTRACT

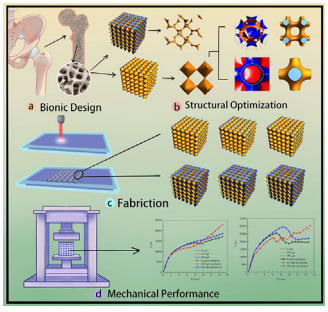

ARTICLE INFO

Article history:
Received 31 March 2023
Revised 15 May 2023
Accepted 19 May 2023
Available online 22 May 2023

Keywords:
Fracture defect
Curvature improvement
Femur-like multimodal surface structure
Superb freedom
Euler theory

ABSTRACT

Based on the microstructure of biological femur, the femur-like multimodal surface structures are designed. But they exhibit fracture behavior when the porosity changes, resulting in structural failure. The high curvature surface factor is introduced to improve the fracture behavior of the biomimetic surface structure. Combine the high curvature surface factor to construct novel biomimetic homogenized surface structures. Novel radial gradient surface structures and axial gradient surface structures are designed based on the construction concept of cone functions and linear functions gradients. Theoretical, experimental and numerical methods are used to investigate the mechanical properties of novel biomimetic multimodal surface structures. Euler theory states that the properties of lattice structures are determined by the relative density of structures. The load distribution in the radially gradient structure is uniform, and the deformation mode presents overall failure, which can achieve better resistance and dissipation of the load. The deformation modes of axial gradient structures present layered failure. The underlying mechanism of the difference in mechanical properties of biomimetic multimodal structures is explained in detail. It's very important significance for targeted application in protective engineering.

1. Introduction

Biomimetic surface structures are support structures found in the microstructures of living organisms that provide necessary

* Corresponding authors.
E-mail addresses: zzxu20@mails.jlu.edu.cn (Z. Xu), zlyu@jlu.edu.cn (Z. Yu).

https://doi.org/10.1016/j.matdes.2023.112018
0264-1275/

support for biological cells and tissues. They are characterized by various distribution forms, such as arrangement distribution, material distribution, hierarchical distribution, etc., as seen in structures like bird beaks, femurs, bamboo, etc. [1,2]. Biomimetic surface structures have multiple surfaces and can be expressed in different forms, such as spatial surface structures or infinite surface structures [3]. Their structural characteristics mainly include volume stability, stress distribution, surface curvature, surface bending degree, flexure, etc. [4–6]. From the mechanical perspective, biomimetic surface structures have great mechanical properties such as durability, bending resistance, compression resistance, torsion resistance, etc. [7]. The structural type, size, and porosity parameters of biomimetic surface structures can be controlled and adjusted through function parameters. By using the functional relationship between porosity and mechanical properties, it is possible to quickly predict the mechanical properties of biomimetic surface structures. Many researchers have studied the mechanical properties of biomimetic surface porous structures [8–10]. Based on density homogenization and interpolation methods, Li et al. [11] optimized the geometric continuity and connectivity of Gyroid to obtain the optimal lightweight lattice structure FGCS with uniform density variation throughout the entire design space. Ronca et al. [12] designed and manufactured a surface porous structure with a high strength-to-weight ratio for efficient energy absorption, which was verified by the elastic isotropic mechanical properties of existing surface structures. Since actual structures are subjected to loading from different directions, Yang et al. [13] discussed the orientation dependence of the mechanical response and structural characteristics of Gyroid under different angles of torsion to ensure the accuracy of uniaxial compression experiments. Zhang et al. [14] obtained the main relationship between the isotropic mechanical properties of various surface structures and their porosity using experimental measurement methods. The mechanical properties of biomimetic surface structures are influenced by multiple factors and are therefore of great importance for engineering design. In future research, it is of great significance to study the mechanical properties of different types of biomimetic surface structures under different external loads and their deformation mechanisms.

However, due to the complex multi-surface configuration of biomimetic surface structures, there are difficulties in the traditional industrial manufacturing of these structures with complex geometries. The development of integrated manufacturing for composite structures is urgently needed [15–17]. Additive manufacturing technology has the advantages of integrated forming, short manufacturing cycle, low manufacturing cost, and high production efficiency. Its development provides an effective solution for the manufacturing needs of complex-shaped structures. With the maturity of additive manufacturing technology, it is replacing traditional manufacturing processes in structural manufacturing and moving towards integrated manufacturing of structures [18–20]. The most commonly additive manufacturing methods include Fused Filament Fabrication (FFF), fused deposition modeling (FDM), Wire Melting Deposition (WMD), and Selective Laser Sintering (SLS) [21]. To better understand the basic geometric characteristics of structures, Tripathi [22] used FDM technology with polylactic acid (PLA) filaments to manufacture and compare the performance of biomimetic surface structures with different porosity. While existing additive manufacturing methods are used to manufacture complex structures, the development of new technologies is also underway. Yang et al. [23] created more flexible and varied shapes for complex surface structures, and prepared and tested a gradient-shaped femur surface structure using novel stereo lithography technology.

However, common additive manufacturing technologies may be limited in the manufacturing of biomimetic surface structures due to the behavior of interfacial fracture defects during their formation. Interfacial fracture defect is a common flaw in biomimetic surface structures, which manifests as a gap between the two endpoints of a surface [24–26]. These gaps can affect structural properties, such as strength and stability, and also affect structural appearance. Therefore, it is important to avoid interfacial fracture defects as much as possible when designing bionic surface structures. In order to better address the impact of interfacial fracture defects in biomimetic surface structures, various new methods of improving surface structures have been proposed. Zhang et al. [27] utilized optimization functions and finite element methods to design and optimize uniform gradient I-Wrapped Package (IWP) structure and Primitive structure, reducing interfacial fracture defects in biomimetic surface structures. However, the reason for the interfacial fracture defect behavior in biomimetic surface structures lies in their own configuration functions. To simplify the optimization process of biomimetic surface structures, Jiang et al. [28] proposed a novel structural adaptive optimization method that significantly improved the configuration stability of gradient surface structures and reduced the impact of interfacial defects in bionic surface structures.

Biomimetic surface structures based on the microstructure of biological femurs exhibit interfacial fracture behavior when porosity changes, leading to structural failure [29]. In this paper, high curvature surface factor is introduced to improve the interfacial fracture behavior of biomimetic function surfaces, and combine the high curvature surface factor to construct novel biomimetic homogenized surface structures: Optimized Gyroid structure (G-opt) and Optimized Primitive structure (P-opt). Furthermore, to investigate the mechanical performance of biomimetic surface structure under multimodal conditions, novel gradient surface structures (Radial gradient optimized Gyroid structure (GR-opt), Axial gradient optimized Gyroid structure (GZ-opt), Radial gradient optimized Primitive structure (PR-opt), Axial gradient optimized Primitive structure (PZ-opt),) are designed by combining the gradient construction concept of the cone function and the linear function. The mechanical properties of novel biomimetic surface structures are studied using theoretical, experimental, and numerical methods, and the energy absorption characteristics of the structures under different forms are analyzed. This paper further investigates the effect of center deviation of central scattering gradient on the mechanical properties.

2. Biomimetic prototype and structural design

The femur is one of the largest bones in the human body, and it has a microstructure characterized by complex surface configurations, including trabeculae, plates, and cortical bone, as shown in Fig. 1 [30]. This microstructure gives the femur some unique mechanical properties, such as being able to provide significant support in resisting impact and torque. At the same time, it forms a "domino" effect that allows the femur to better distribute and absorb forces when subjected to external forces [31]. Meanwhile, the microstructure of the femur gives it excellent mechanical properties, including strength, stiffness, and wear resistance. These properties allow the femur to bear much of the body weight and loads required for movement, providing strong support [32].

In this paper, two biomimetic surface structures are constructed based on the microstructure of the femur surface [33]. The biomimetic configuration functions are shown in Eq. (1) and Eq. (2), and the biomimetic models are illustrated in Fig. 1(b) (c).

$$D_G = \sin a_G x \cos b_G y + \sin b_G y \cos c_G z + \sin c_G z \cos a_G x \tag{1}$$

$$D_I = \cos(a_I x)\cos(b_I y) + \cos(b_I y)\cos(c_I z) + \cos(c_I z)\cos(a_I x) \tag{2}$$

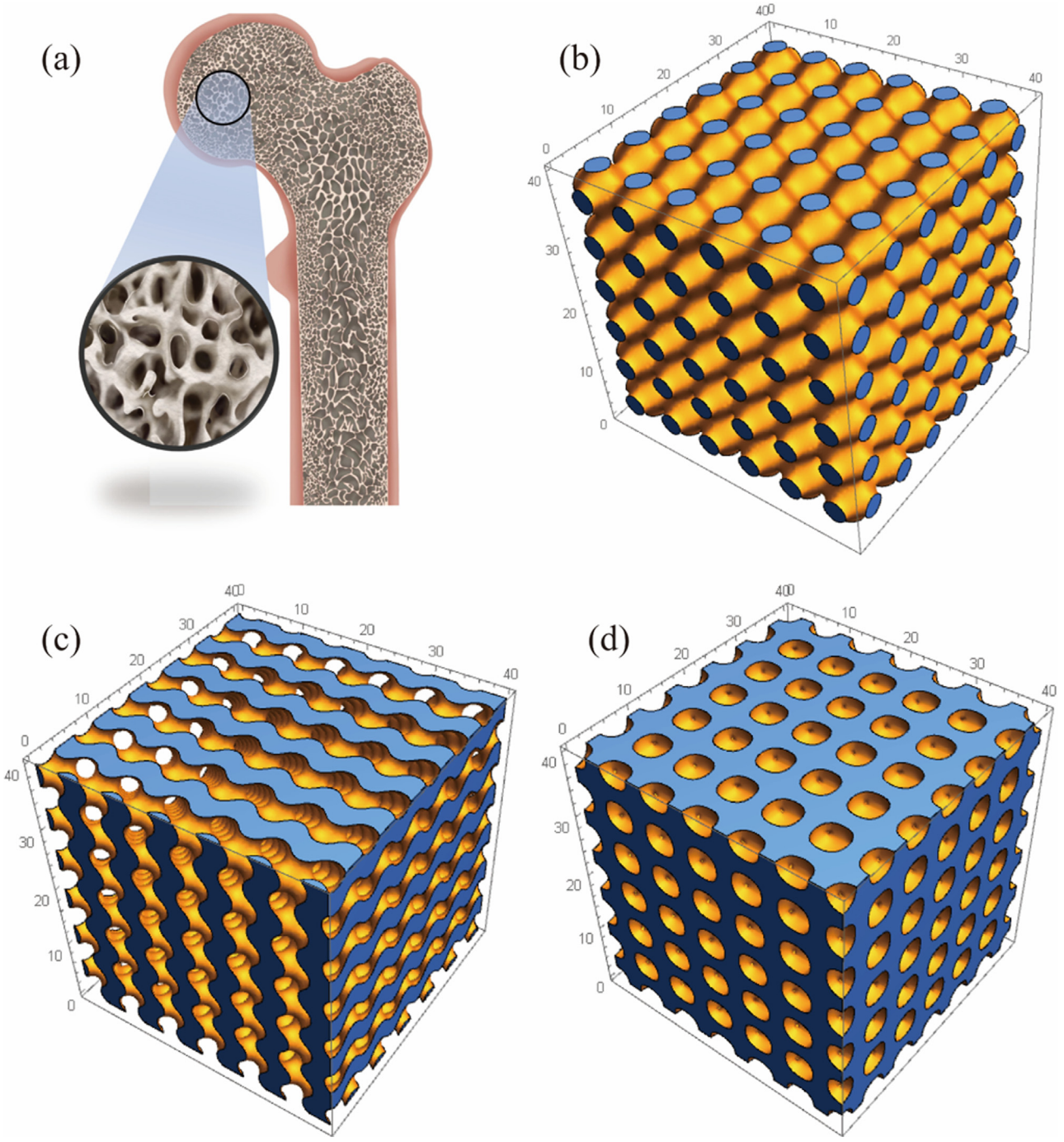

Fig. 1. Design of biomimetic surface structures. (a) The femur. (b) Primitive. (c) Gyroid. (d) IWP.

$$D_P = \cos(a_P x) + \cos(b_P y) + \cos(c_P z) \quad (3)$$

where, G, I, and P are Gyroid, IWP, and Primitive. D_G, D_I, and D_P can be used to adjust the volume fraction of the bionic surface porous structure, respectively. a_i, b_i, b_i, i = G, I, P represent the period in the x, y, z directions of the different structural surface functions. $a_i = 2\pi\frac{n_{a_i}}{L_{a_i}}$, $b_i = 2\pi\frac{n_{b_i}}{L_{b_i}}$, $c_i = 2\pi\frac{n_{c_i}}{L_{c_i}}$; n_r, $r = a_i, b_i, c_i$ respectively represent the number of units in the x, y, and z directions of the bionic surface structure.L_r is the total length of the bionic surface structure in different directions.

However, the biomimetic surface structures exhibit cutoff defect behavior as porosity changes, as shown in Fig. 2. Primitive exhibits severe cutoff defects at a porosity of 80%, while Gyroid exhibits severe cutoff defect behavior at a porosity of 95%. This leads to lower compressive performance in terms of structural properties, as shown in Fig. 2(b) (d). At the same time, the unevenness of surface bending curvature also leads to defects in structural performance.

To mitigate the interfacial fracture behavior of biomimetic surface structures caused by increasing porosity, this paper combines the high curvature characteristics of the IWP surface intersection. The IWP function is constructed as shown in Eq. (3), and IWP is shown in Fig. 1(c). The detailed transformation principle is shown in Fig. 2.

As the interfacial fracture behavior is caused by excessively small surface curvature, it can be improved by increasing the

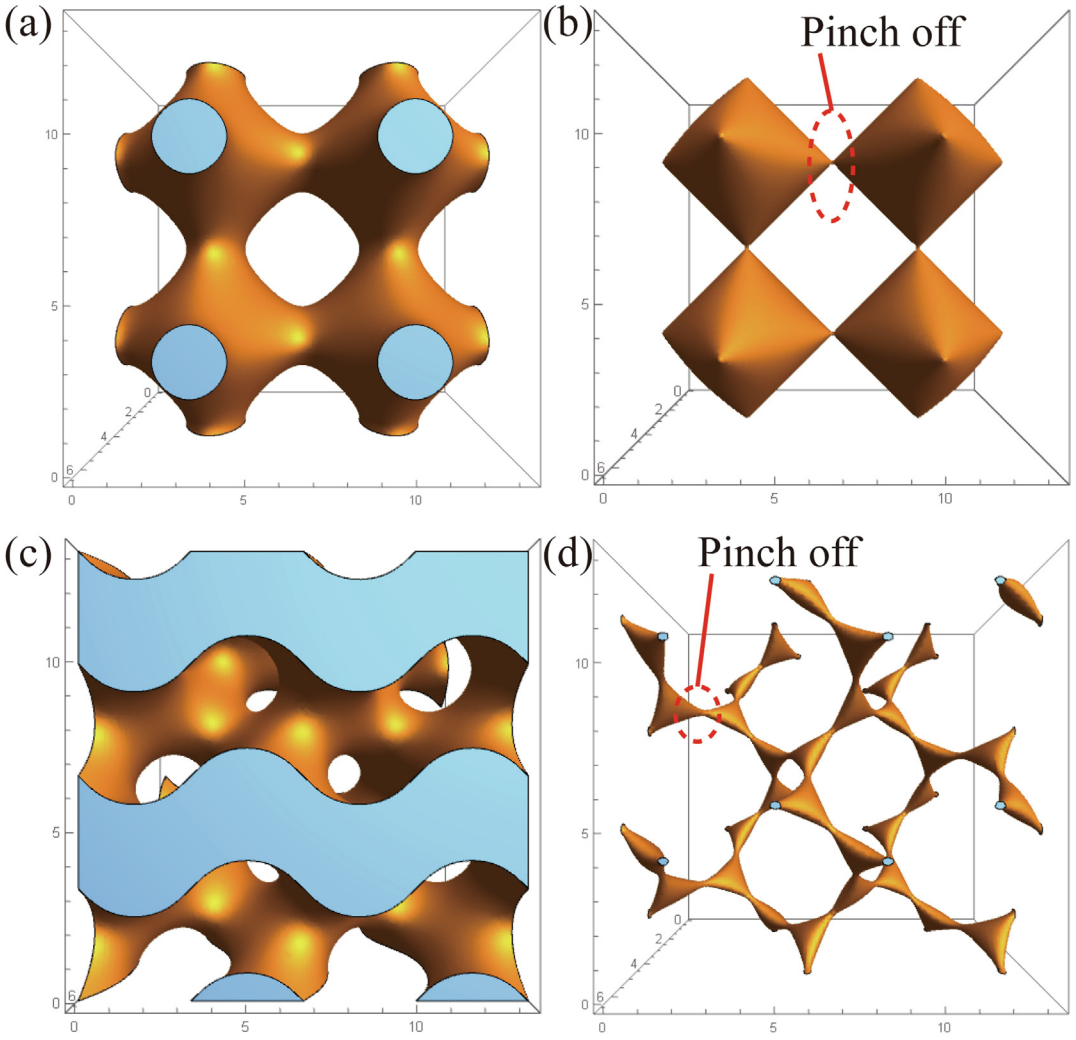

Fig. 2. Biomimetic surface structure with interfacial fracture behavior. (a) Original Primitive. (b) Original Gyroid. (c) Interfacial fracture behavior of Primitive. (d) Interfacial fracture behavior of Gyroid.

surface curvature. Take the improvement of Primitive as an example to illustrate. IWP surface and Primitive surface are superimposed in the same coordinate system, as shown in Fig. 3(a). It can be seen that the main part of IWP surface and Primitive surface present a complementary state. This complementary configuration causes the surface coordinate points to approach the IWP surface, thereby enhancing the curvature of the surface. As shown in Fig. 3 (b), the coordinate points of the Primitive surface are approaching the vicinity of the dashed line. It can be clearly seen that the curvature of the structural surface has been significantly improved, and the porosity of the improved structure can reach 99 %, as shown in Fig. 3(c) (d). The curvature increases at the units' intersection, and the improved structure has a larger curvature transition, which mitigates the impact of structure interruption on production and application, as indicated by the circled areas in Fig. 3 (c) and Fig. 2 (a). The specific improved surface functions are given by Eqs. (4) and (5).

$$D_{P\text{-}opt} = m_{P\text{-}opt}\left[\cos\left(a_{P\text{-}opt}x\right) + \cos\left(b_{P\text{-}opt}y\right) + \cos\left(c_{P\text{-}opt}z\right)\right] + n_{P\text{-}opt}\left[\cos\left(a_{P\text{-}opt}x\right)\cos\left(b_{P\text{-}opt}y\right) + \cos\left(b_{P\text{-}opt}y\right)\cos\left(c_{P\text{-}opt}z\right) + \cos\left(c_{P\text{-}opt}z\right)\cos\left(a_{P\text{-}opt}x\right)\right] \tag{4}$$

$$D_{G\text{-}opt} = m_{G\text{-}opt}\left[\sin\left(a_{G\text{-}opt}x\right)\cos\left(b_{G\text{-}opt}y\right) + \sin\left(b_{G\text{-}opt}y\right)\cos\left(c_{G\text{-}opt}z\right) + \sin\left(c_{G\text{-}opt}z\right)\cos\left(a_{G\text{-}opt}x\right)\right] + n_{G\text{-}opt}\left[\cos\left(a_{G\text{-}opt}x\right)\cos\left(b_{G\text{-}opt}y\right) + \cos\left(b_{G\text{-}opt}y\right)\cos\left(c_{G\text{-}opt}z\right) + \cos\left(c_{G\text{-}opt}z\right)\cos\left(a_{G\text{-}opt}x\right)\right] \tag{5}$$

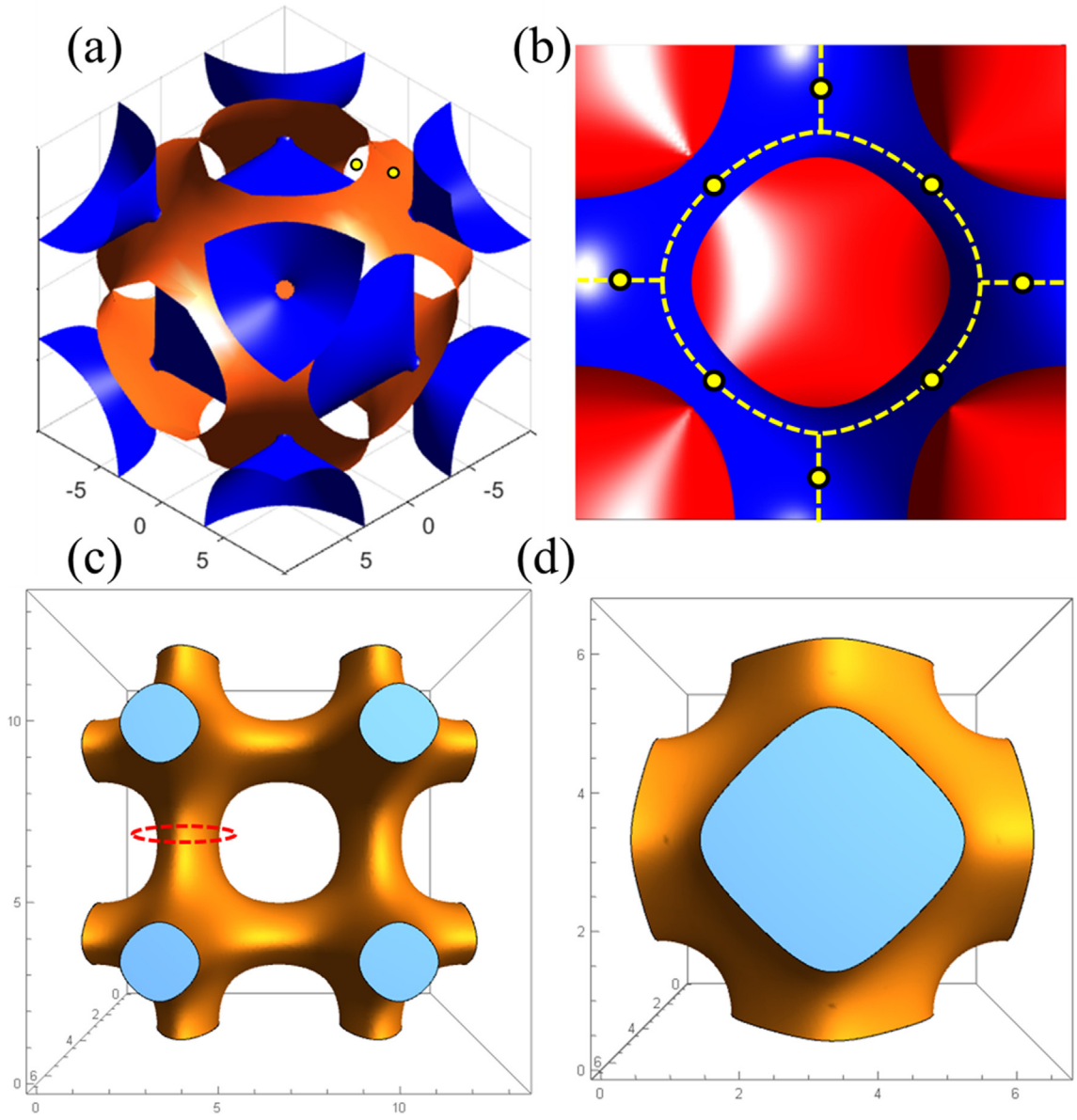

Fig. 3. Transformation principle of the interfacial fracture behavior of the bionic surface structure. (a) Improved function surface and original function surface. (b) Improved principle of surface coordinate movement. (c) Improved Primitive. (d) Improved Primitive unit.

where, $m_{\text{P-opt}}$, $n_{\text{P-opt}}$, $m_{\text{G-opt}}$, and $n_{\text{G-opt}}$ are constants representing the curvature of the transition section of the surface.

To better understand the influence of the gradient change in structural porosity on the mechanical properties of the bionic surface structure, a novel bionic axial gradient surface structure function is constructed by modifying D_i into a linear function related to the unidirectional z coordinate, $D_u = c_u + d_u z, u = \text{G - opt}, \text{P - opt}$. The size of the improved axial gradient surface structure is 40 × 40 × 40 mm. The number of lattice units is 6 × 6 × 6 in the x, y, and z directions. The axial porosity varies from 31.5% to 55.5%, as shown in Fig. 4(b) (e). The design parameters of the improved axial gradient surface structure are shown in Table 1.

Similarly, D_i is replaced with the conical function to construct novel radial gradient femur-like surface structure function, $D_v = e_v + f_v\sqrt{x^2 + y^2}, v = \text{GR - opt}, \text{PR - opt}$. The size of the improved radial gradient surface structure is 40 × 40 × 40 mm. The number of lattice units is 6 × 6 × 6 in the x, y, and z directions. The radial porosity varies from 31.5 % to 55.5 %, as shown in Fig. 4 (c) (f). The design parameters of the improved radial gradient surface structure are shown in Table 2.

Establish the parameter $D_i = \alpha_1 x + \alpha_2 y + \alpha_3 z + \beta_1 x^2 + \beta_2 y^2 + \beta_3 z^2 + \gamma_1 xy + \gamma_2 yz + \gamma_3 zx$, where x, y, and z are coordinates and α_δ, β_δ, and γ_δ are the constant, $\delta = 1,\ 2,\ 3$. During compression of the structure, output the stress and corresponding coordinate, and establish a functional relationship between stress and coordinates using interpolation, where $\sigma = \eta_1 x + \eta_2 y + \eta_3 z + \kappa_1 x^2 + \kappa_2 y^2 + \kappa_3 z^2 + \vartheta_1 xy + \vartheta_2 yz + \vartheta_3 zx$, where x, y, and z are coordinates and η_δ, κ_δ, and ϑ_δ are the constant,. The porosity $\Im$ and the bearing stress σ have a linear relationship, that is, $\sigma = \varpi\Im$, where ϖ is a constant. The structure porosity at different positions can be directly adjusted according to the coordinates, that is, $D_i = \Im = (\eta_1 x + \eta_2 y + \eta_3 z + \kappa_1 x^2 + \kappa_2 y^2 + \kappa_3 z^2 + \vartheta_1 xy + \vartheta_2 yz + \vartheta_3 zx)/\varpi$. Thus, multimodal ultrahigh strength structures with superb freedom are achieved, as shown in Attachment 2.

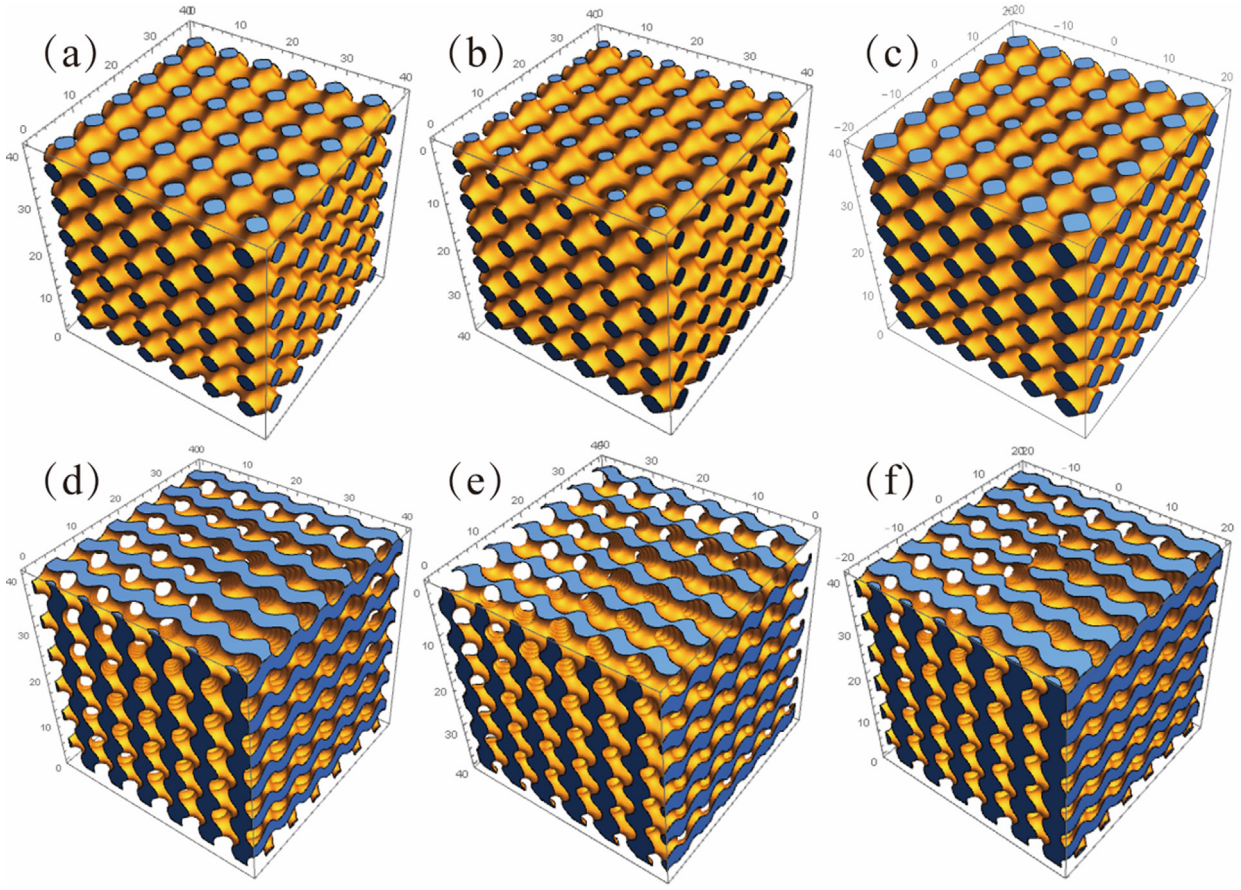

Fig. 4. Novel multimodal biomimetic surface structures. (a) P-opt. The porosity is 43.5%. (b) PZ-opt. (c) PR-opt. (d) G-opt. The porosity is 43.5%. (e) GZ-opt. (f) GR-opt. Write and output novel multimodal biomimetic surface structures using Matlab software, as shown in Attachment 1.

Table 1
The design parameters of the improved axial gradient surface structure.

	a	b	c	m	n	c	d
PZ-opt	0.25	0.25	0.25	4	2	−4	0.05
GZ-opt	0.25	0.25	0.25	10	4	−6.08	0.2

Table 2
The design parameters of the improved radial gradient surface structure.

	a	b	c	m	n	e	f
PR-opt	0.3	0.3	0.3	4	2	−4.28	0.145
GR-opt	0.3	0.3	0.3	10	4	−8.1	0.4

3. Structural additive manufacturing and material parameter characterization

The generated STL models are imported into the FS300 selective laser sintering (SLS) printer to efficiently print eight types of multi-morphology novel biomimetic surface structure samples, as shown in Fig. 5(a). The SLS process is carried out under argon protection to ensure that the oxygen content is less than 300 ppm. The diameter of the 3D printer nozzle is 0.4 mm. The scanning speed of the SLS process is 1000 mm/s, and the power range of the disk laser is 110–180 W. The precision is 0.6 mm. The specific 3D-printing parameters are shown in Table 3.

At room temperature (RT, ~298.15 K), XRD characterization shows that the powder composition is Nylon phase and no other secondary phases are observed, as shown in Fig. 5(b). The microstructure of Nylon powder is shown in Fig. 5(c), and it can be seen that most of the powder particles are regular spheres. Nylon powder is prepared by solvent precipitation method, with the particle size range of 10 ~ 100 μm, as shown in Fig. 5(d). Orthogonal stacking can occur on the powder bed (composite stacking of large particle size powder and small particle size powder), which reduces the porosity of the powder bed and improves the quality of model forming [34].

Material tensile and compressive experiments are conducted on Nylon samples using a universal testing machine (Instron 5963), as shown in Fig. 6. The testing speeds are set at 1 mm/min for tensile testing and 0.5 mm/min for compressive testing. Each sample is tested three times, and the test results are averaged. The constitutive material of the models is Nylon, with the following material properties: density of 1100 kg/m^3, elastic modulus of 1000 MPa,

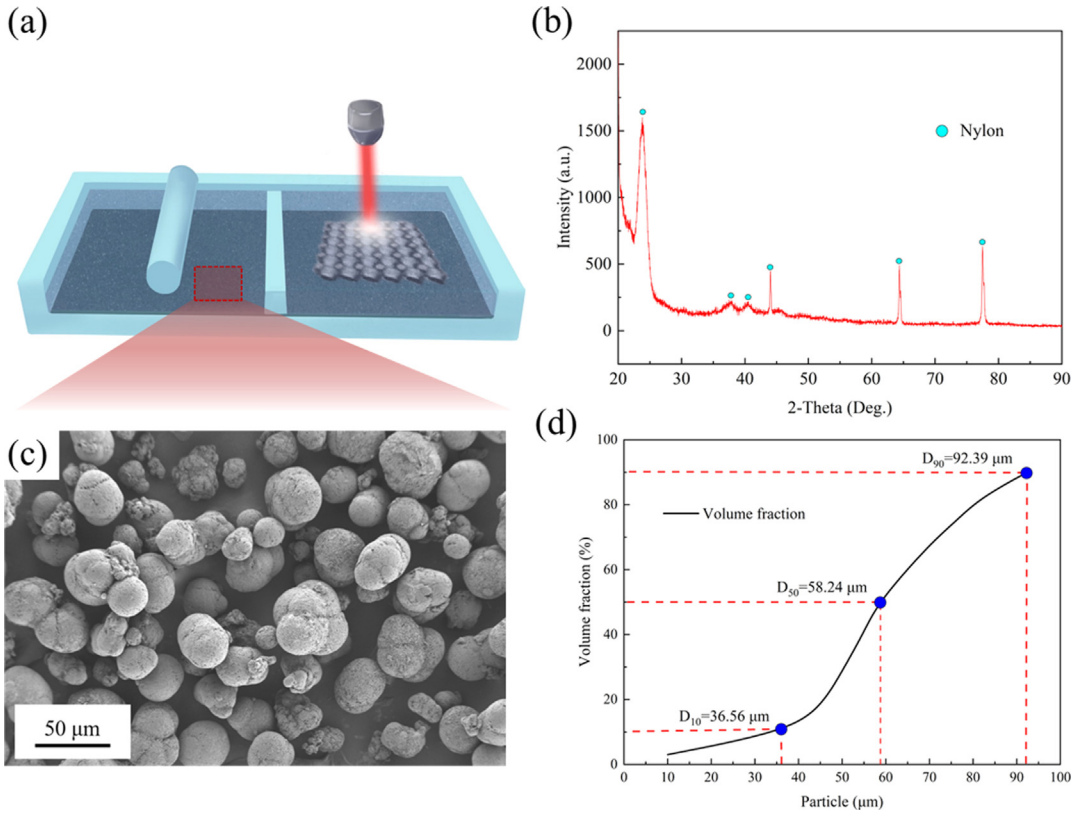

Fig. 5. Additive manufacturing process and material samples analysis. (a) SLS manufacturing process. (b) XRD curve of Nylon powder. (c) Cumulative distribution of Nylon powder size. (d) Microscopic morphology of Nylon powder.

Table 3
3D-printing parameters.

Parameters	Scanning speed (mm/s)	Build cavity temperature (°C)	Laser power (W)	Preheating temperature (°C)	Jumping speed (mm/s)
Tensile sample	7.62	169	22	140	2.54

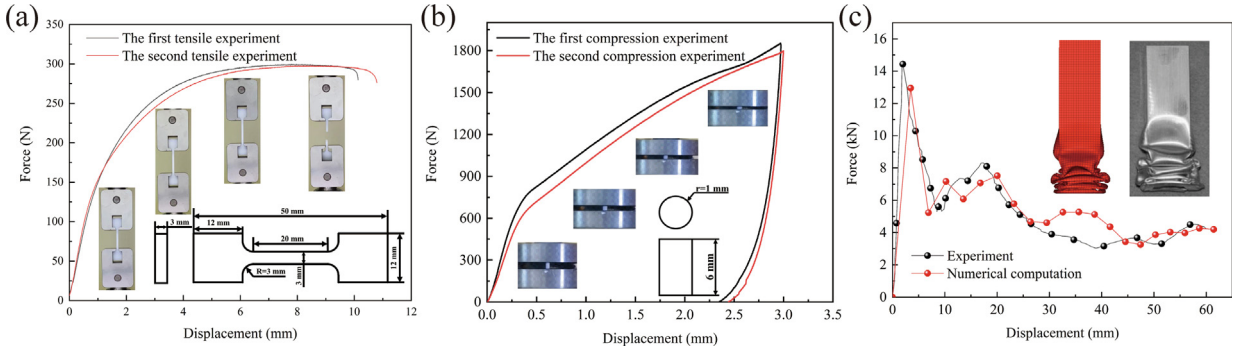

Fig. 6. Results of material property testing. (a) Tensile testing results of nylon. (b) Compressive testing results of nylon. (c) Property testing results of aluminum alloy square tube [37].

and Poisson's ratio of 0.33. The compression and tensile relationship of Nylon is characterized by an ideal elastic–plastic constitutive model, and the specific material property results are shown in Fig. 6(a) (b). Due to the strain sensitivity of nylon, materials with low strain sensitivity, such as aluminum alloy [35], are used for impact testing of porous structures. Aluminum alloy can effectively reduce the influence of strain rate, ensuring the accuracy and reliability of impacting data. The density of aluminum alloy is 2700 kg/m^3. Its elastic modulus is 69.3 GPa. Poisson's ratio is 0.33, and its static yield strength is 258 MPa [36]. The accuracy of the properties of the aluminum alloy material is verified through square tube simulation, as shown in Fig. 6(c).

The nonlinear dynamic finite element program LS-DYNA is used to simulate the quasi-static compression response and impact

response of surface porous structures. The bionic surface structure is placed on a fixed rigid plate with six degrees of freedom constraints, and quasi-static compression is performed in the z direction by another movable rigid plate, as shown in Fig. 7. However, due to the excessively high computational cost of simulating the loading speed (1 mm/min) analogous to quasi-static compression experiment, the speed of v = 0.01 m/s is assigned to the movable rigid plate to ensure the accuracy and efficiency of quasi-static compression simulation [34]. # Surface-to-surface contact and # Self-contact algorithm are defined to simulate the contact behavior between different parts of the bionic surface structure after compression deformation. The friction coefficient between the dynamic simulation is 0.15 [38].

4. Structural mesh sensitivity analysis

In order to decide on the optimal elements' dimensions of the structural components, the sensitivity analysis is performed. Single lattice of G-opt and P-opt is meshed using Tet solid element in LS-DYNA. By subjecting bio-inspired lattice to the compression of 3 mm, the total absorbed energy of the bio-inspired structures is depicted in Fig. 8.

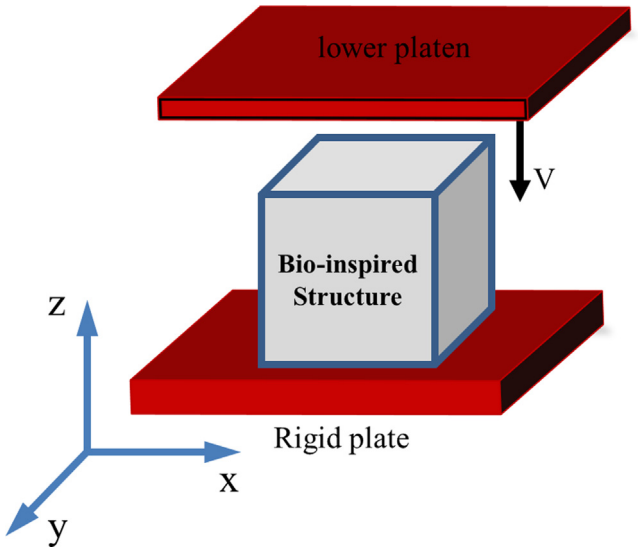

Fig. 7. Structural Compression Simulation.

As shown in Fig. 8(a), the evolution of structural compressive absorbed energy with the change of mesh size is extracted for different element sizes. Compared with the ultra-fine mesh size of 0.5 mm, the models with structural mesh sizes of 0.75 mm and 1 mm can generate very similar results. However, the deviation of the structural compressive absorbed energy increases as the structural mesh size increases. The required time for structural compression simulation with size variation running on a 4-core Intel (R) Core (TM) i7-7500U CPU @ 2.70 GHz is shown in Fig. 8 (a). As the mesh size gradually increases, the computational time cost gradually decreases. Based on the results of Fig. 8, it is apparent that the simulation elements should be sized at 1 mm.

5. Characteristic analysis of multimodal biomimetic surface structures

5.1. Theoretical prediction of complex structures

The lattice structure undergoes elastic deformation during initial compression. For quasi-static compression (extremely small structural strain rate) and relative density greater than 0.1 [38], Euler theory can be used to calculate the deformation of the lattice structure. The micro-deformation of the structural beam is determined.

$$\Delta L = \frac{FL^3}{E_S I} \tag{6}$$

$$I = \frac{t^4}{12} \tag{7}$$

where, E_S is the material elastic modulus. t is the width of beam. L is the length of beam.

The structural elastic modulus is

$$E = \frac{\sigma}{\varepsilon} = \zeta \frac{E_S I}{SL^2} \tag{8}$$

$$\sigma = \frac{F}{S} = \frac{\Delta L E_S I}{SL^3} \tag{9}$$

$$\varepsilon = \frac{\Delta L}{L} \tag{10}$$

where, ζ is the constant.

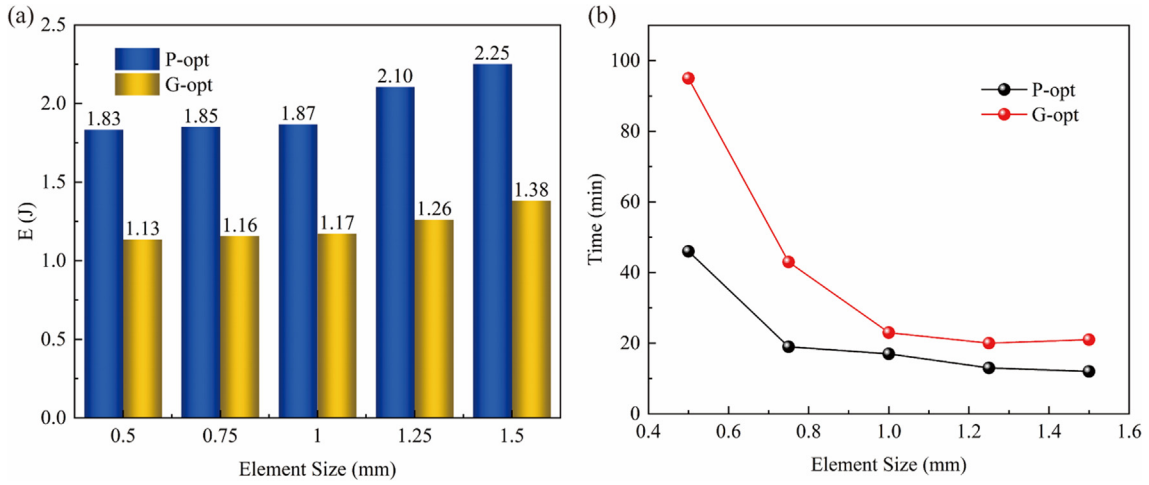

Fig. 8. The structural mesh sensitivity analysis. (a) Structural compressive absorbed energy with size variation. (b) Structural compressive simulation time with size variation.

The structural relative density is

$$\frac{\rho}{\rho_S} = \frac{M/V}{M/V_S} = \frac{V_S}{V} \tag{11}$$

where, The structural actual volume $V_S \propto Lt^2$. The structural space volume is $V = L^3$, ρ is the density of the lattice structure. ρ_S is the material density of Nylon.

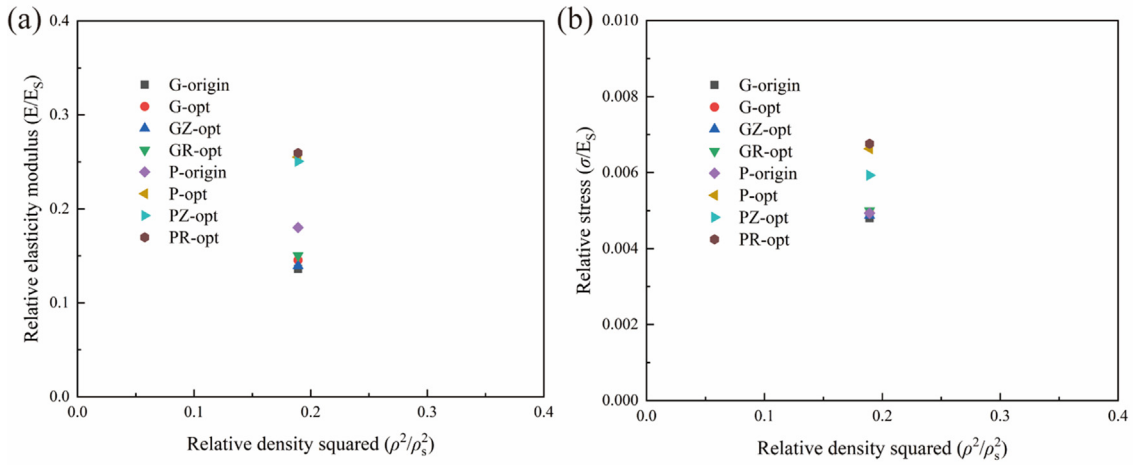

Fig. 9. Theory Results. (a) The relation between relative elastic modulus E/E_S and relative density ρ^2/ρ_S^2. (b) The relation between bending stress σ/E_S and relative density ρ^2/ρ_S^2.

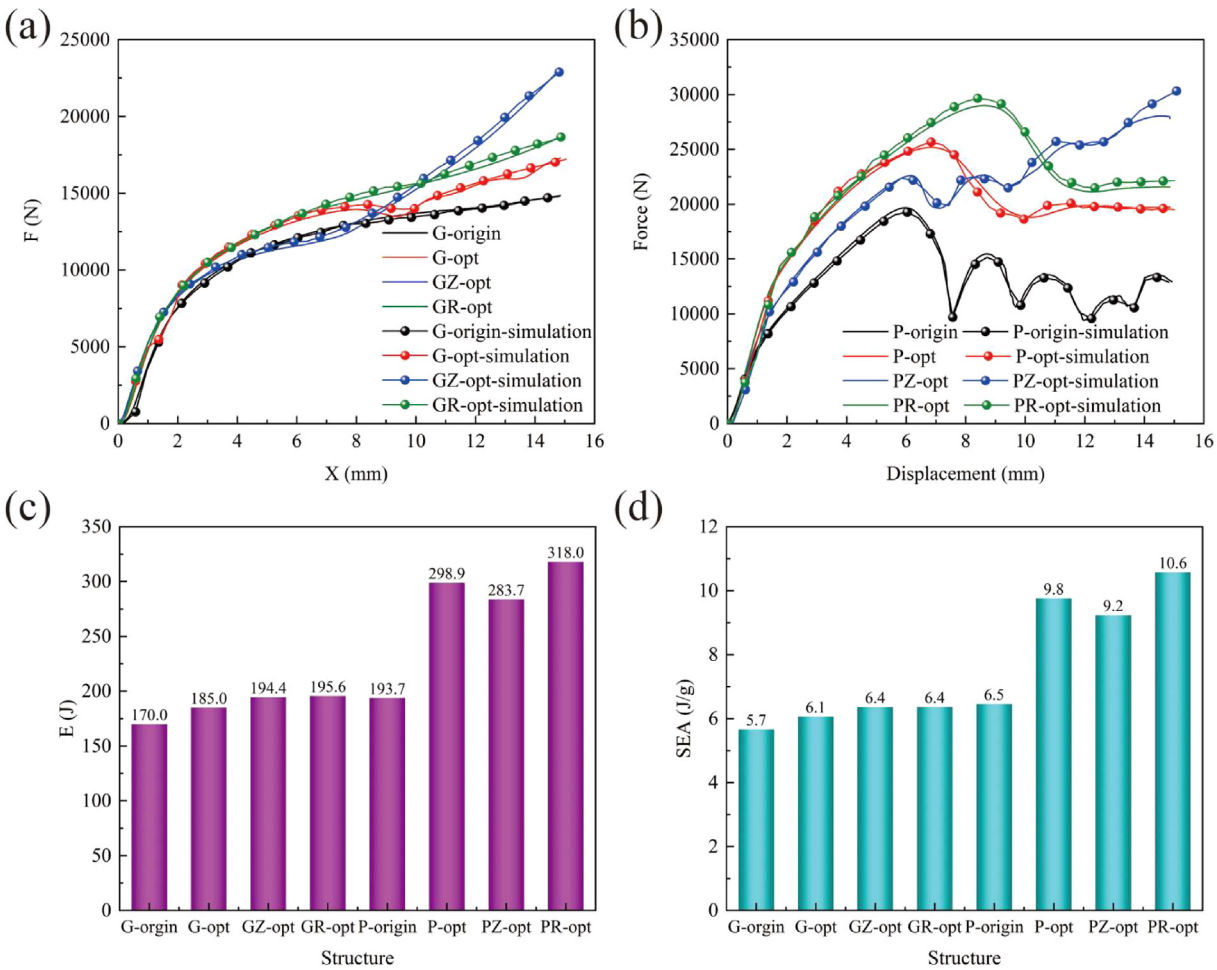

Fig. 10. Quasi-static compression results. (a) Compressive force–displacement curve of multimodal biomimetic Gyroid. (b) Compressive force–displacement curve of multimodal biomimetic Primitive. (c) E of multimodal biomimetic structures. (d) SEA of multimodal biomimetic structures.

$$\frac{\rho}{\rho_S} \propto \left(\frac{t}{L}\right)^2 \tag{12}$$

So,

$$\frac{E}{E_S} \propto \left(\frac{\rho}{\rho_S}\right)^2 \tag{13}$$

That is

$$\frac{E}{E_S} = A_1\left(\frac{\rho}{\rho_S}\right)^2 + B_1 \tag{14}$$

where, A_1 and B_1 are the constants.

Similarly, the structural bending force is

$$F = a\frac{n^2\pi E_S I}{L^2} \tag{15}$$

where, n = 0.7 [39]. a is the constant.

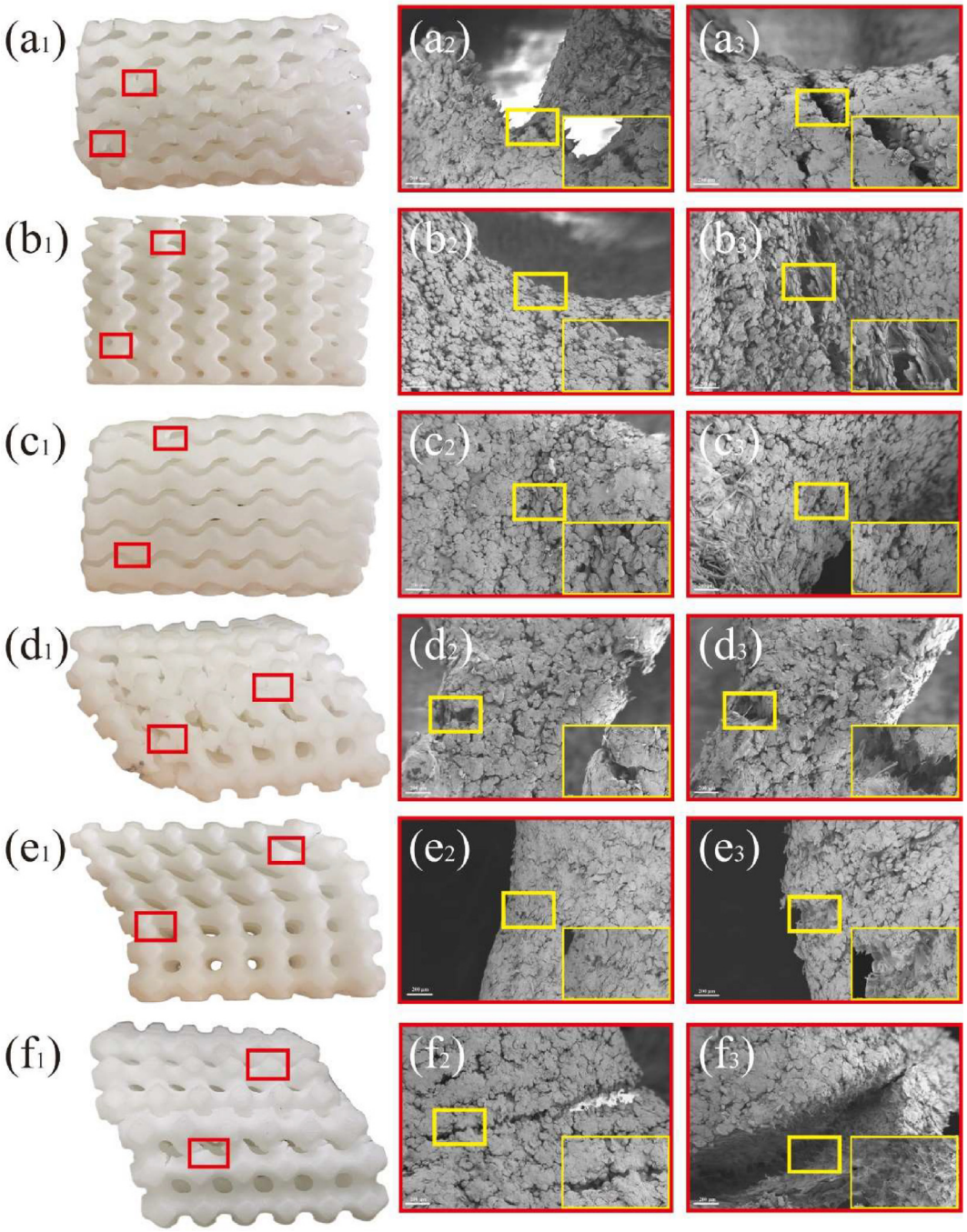

Fig. 11. The deformation and damage mechanisms of multimodal biomimetic structures. (a_1) The deformation mode of G-opt under engineering compression strain of 34.5 %. ($a_{2\text{-}3}$) SEM figures of G-opt under engineering compression strain of 34.5 %. (b_1) The deformation mode of GZ-opt under engineering compression strain of 34.5 %. ($b_{2\text{-}3}$) SEM figures of GZ-opt under engineering compression strain of 34.5 %. (c_1) The deformation mode of GR-opt under engineering compression strain of 34.5 %. ($c_{2\text{-}3}$) SEM figures of GR-opt under engineering compression strain of 34.5 %. (d_1) The deformation mode of G-opt under engineering compression strain of 34.5 %. ($d_{2\text{-}3}$) SEM figures of P-opt under engineering compression strain of 34.5 %. (e_1) The deformation mode of G-opt under engineering compression strain of 34.5 %. ($e_{2\text{-}3}$) SEM figures of PZ-opt under engineering compression strain of 34.5 %. (f_1) The deformation mode of G-opt under engineering compression strain of 34.5 %. ($f_{2\text{-}3}$) SEM figures of PR-opt under engineering compression strain of 34.5 %.

Therefore, the structural load is under compression deformation.

$$\sigma \propto \frac{F}{L^2} \propto \frac{E_S I}{L^4} \tag{16}$$

Combine (7) and (12),

$$\frac{\sigma}{E_S} \propto \frac{t^4}{L^4} \propto \left(\frac{\rho}{\rho_S}\right)^2 \tag{17}$$

So

$$\frac{\sigma}{E_S} = A_2\left(\frac{\rho}{\rho_S}\right)^2 + B_2 \tag{18}$$

where, A_2 and B_2 are the constants.

The theory results of structures are shown in Fig. 9.

The structural performance is directly related to the relative density, and complex structures with the same relative density have similar elastic modulus and bending stress, as shown in Fig. 9. However, the structural performance is directly correlated with structural form after reaching the bending stress, as shown in Fig. 10.

5.2. Analysis indicators

To achieve precise and quantitative assessment of the protective capabilities of the bio-inspired structure, various evaluation parameters are employed, including energy absorption *EA* and specific energy absorption *SEA* [40].

The energy absorption resulting from the structural deformation caused by the compression of the rigid wall is computed using Eq. (19).

$$EA = \int_0^{x_0} F\mathrm{d}x \tag{19}$$

where, x_0 represents the total displacement caused by quasi-static compression, while *F* denotes the quasi-static payload applied during compression.

SEA refers to crucial parameters that measure the energy absorption capacity per unit mass and per unit volume. This is demonstrated in Eq. (20).

$$SEA = \frac{EA}{M} \tag{20}$$

where, *M* is the structural mass and *V* is the structural volume. The significance of *SEA* in protective design cannot be overstated, as it plays a crucial role in ensuring the effectiveness of protective engineering. High *SEA* values are especially critical in such applications, as they indicate a greater capacity for energy absorption, thereby enhancing the protective capabilities of the structure.

5.3. Compression characteristics analysis of multimodal biomimetic surface structure

Simulations and evaluations are conducted on the compression characteristics of multimodal biomimetic surface structures. The rigid base is fixed at the bottom of structures, and a rigid plate compresses the multimodal biomimetic surface structure from the top at a constant speed to evaluate its compression and fracture response. The results are processed into force–displacement curves and energy absorption figures, and comparison figures are drawn with the experimental results as shown in Fig. 10.

Fig. 10(a) and (b) show the force–displacement curves under quasi-static compression, and it is evident from the figures that structural compression response is characterized by two distinct stages. The curve begins with the linear elastic stage, followed by a long flat plateau. After the initial elastic stage, structures exhibit plastic deformation and absorb energy under relatively constant stress. However, in the axial gradient models, the force–displacement curve remains steadily increasing or shows a step-like increase due to the increased self-contact area between the walls of each layer. Moreover, there is good agreement between all repeated experiments, and the experimental and simulated results have high reliability with a similarity degree of over 90%.

The multimodal biomimetic structures are sequentially compressed to a strain of 34.5%, and observed for damage by scanning electron microscopy (SEM). Fig. 11 shows the damage patterns in different regions of biomimetic structures. The strain of the upper, middle and lower layers of G-opt, GZ-opt, and GR-opt is similar. After the overall cracking occurs, the force increases slowly, as shown in Fig. 10(a). During the structural compression, the strain of P-opt, PZ-opt, and PR-opt in the upper, middle and lower layers is different, with a decreasing strain from top to bottom. The damaged area shows structural bending and cracking (Fig. 11($a_{1\text{-}3}$) ($b_{1\text{-}3}$) ($c_{1\text{-}3}$)). The strain region of P-opt, PZ-opt, and PR-opt shows that structures are bent, which led to the extension of cracks and then twisting and structural fracture. The structural strain region experienced tearing, resulting in a decrease in force in the force–displacement curve, as shown in Fig. 10b). Since the structural cracking further merges, connects, and expands with compression [41], structures do not suffer severe destruction as a whole and remain intact, which greatly retain the carrying capacity, and keep their load stable, as shown in Fig. 10(a) (b).

Micro-voids are preferentially produced when the structure fractures. With the deformation of the structure, micro-voids nucleate, grow, slip, and aggregate to form a ductile dimple frac-

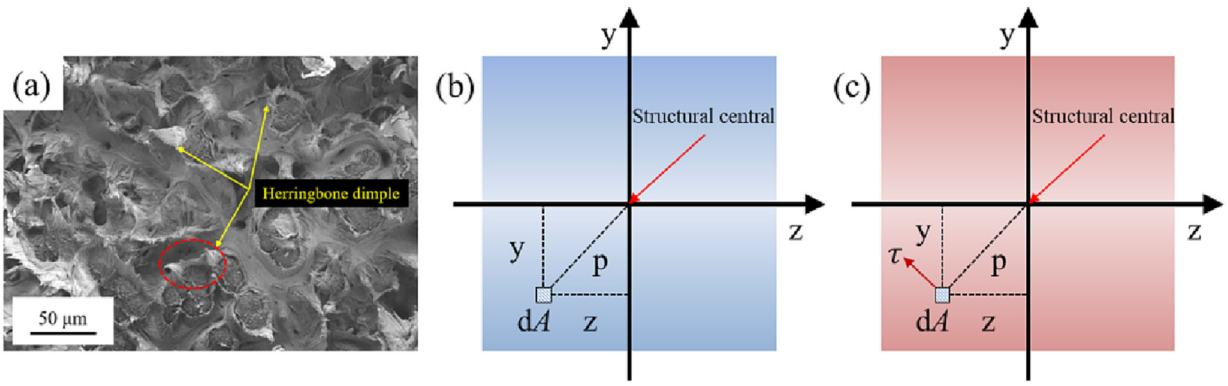

Fig. 12. Principle of structural section analysis. (a) Microscopic morphology of Nylon fracture surface. (b) Bending stress of section. (c) Torsional stress of section.

ture, as shown in Fig. 12(a). The irregular distribution of internal crack leads to an increase in crack propagation resistance during fracture. Multiple steps are generated during the process of crack propagation, resulting in a rough surface of the fracture and increased energy consumption. In the ductile dimple at the compression fracture surface, the fiber direction is consistent and presents a distinct herringbone pattern. However, there are also some small ductile dimples with fibers torn in other directions, as shown in Fig. 12(a). This further indicates that the fracture site is subjected to uniaxial bending and torsional loads, and loading position is the junction part of the structural unit.

In essence, different types of structures have different bearing capacities. The bending section modulus of the structure is

$$W_z = \frac{I_z}{y_{\max}} \tag{21}$$

where the moment of inertia of the section is

$$I_z = \int_A p^2 \mathrm{d}A = \int_A (z^2 + y^2)\mathrm{d}A \tag{22}$$

A is the cross-sectional area of biomimetic surface structure in the direction of compression. The detailed schematic is shown in Fig. 12(b) (c).

$$\sigma_{z\max} = \frac{M_z}{W_z} = \frac{M_z y_{\max}}{\int_A (z^2 + y^2)\mathrm{d}A} \tag{23}$$

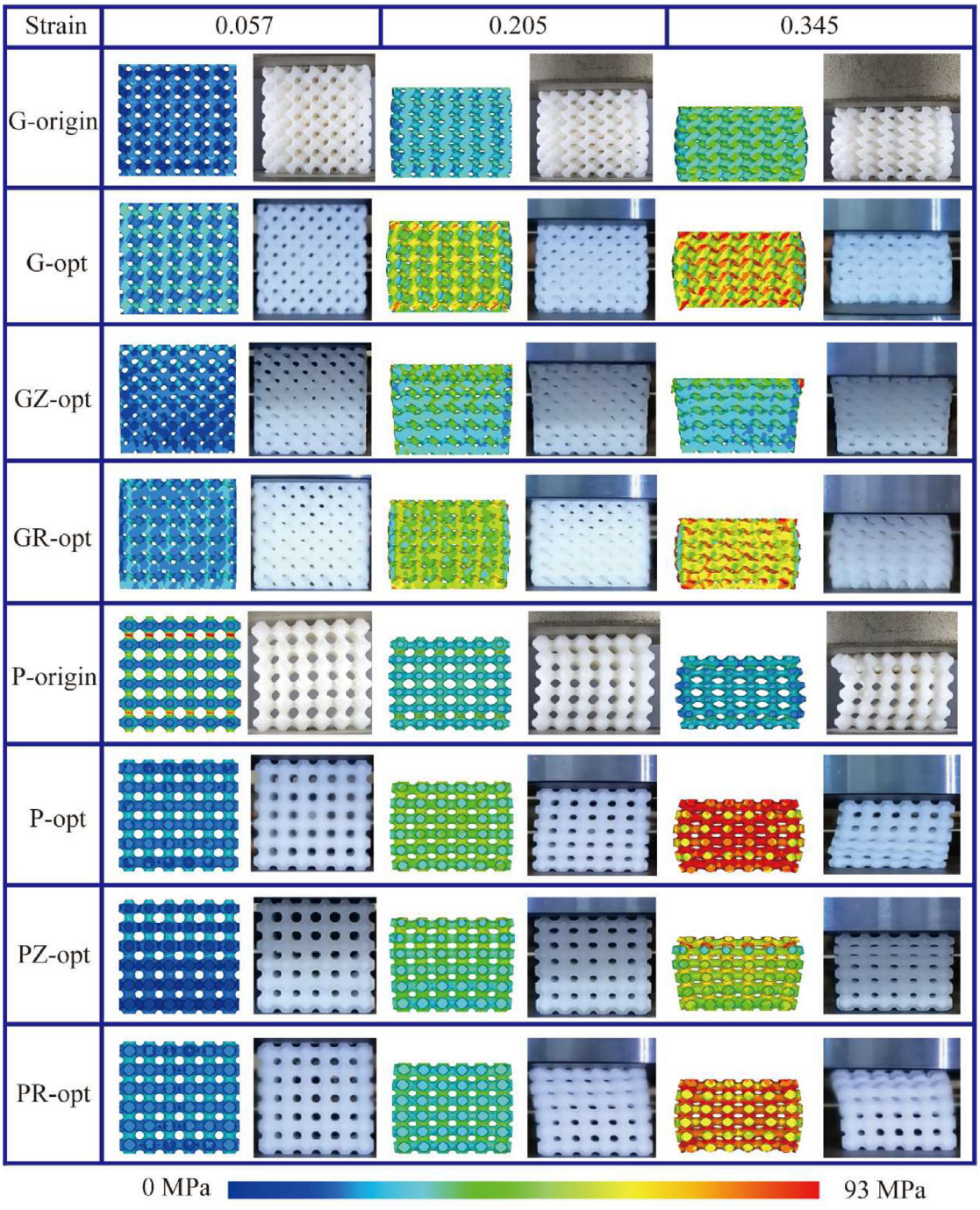

Fig. 13. Structural compression deformation modes.

where, M_z is the structural moment around the z-axis.

Similarly, the bending stress around the y-axis is

$$\sigma_{y\max} = \frac{M_y}{W_y} = \frac{M_y z_{\max}}{\int_A (z^2 + y^2) dA} \tag{24}$$

The sum of all the micro torque forces on the cross-section is the total torque of the structural cross-section. That is

$$T = \int_A p\tau_p dA \tag{25}$$

The torsion section coefficient of biomimetic surface structure is

$$W_t = \frac{I_t}{p_{\max}} \tag{26}$$

where, the polar moment of inertia of the section is

$$I_t = \int_A p^2 dA = \int_A (x^2 + y^2) dA \tag{27}$$

Structural torsional stress is

$$\tau_{\max} = \frac{T}{W_t} = p_{\max} \int_A \frac{p\tau_p}{(x^2 + y^2)} dA \tag{28}$$

At the same height, the cross-sectional area of the radial gradient structure and uniform structure is the same, and the cross-sectional area of axial gradient structure is small. However, the cross-sectional area of axial gradient structure increases layer by layer. The original structure has a minimum cross-sectional area at the junction of the units, as shown in Fig. 2(a) and Fig. 3(c). At the same time, the radial gradient structure has a higher p than the uniform structure. So structural bending stress satisfies $\sigma_R > \sigma_U > \sigma_A > \sigma_{Origin}$. Where, σ_R is the bending stress of radial gradient structure. σ_U is the bending stress of uniform axial gradient structure. σ_A is the bending stress of axial gradient structure. σ_{Origin} is the bending stress of original structure. Similarly, structural torsional stress satisfies $\tau_R > \tau_U > \tau_A > \tau_{Origin}$. As compression occurs, the cross-sectional area of the load-bearing position in the axial gradient structure increases and is greater than that of the radial gradient structure and uniform structure. According to Eq. (23), Eq. (24), and Eq. (28), the bending stress of the structure satisfies $\sigma_A > \sigma_R > \sigma_U > \sigma_{Origin}$, and structural torsional stress satisfies $\tau_A > \tau_R > \tau_U > \tau_{Origin}$. Fundamentally explaining the changes in load capacity of structures with different shapes is consistent with the trends observed in experimental and simulation results.

Comparing each biomimetic surface structure, it is evident that the radial gradient structure outperforms original structure, uniform structure and axial gradient structure in terms of energy absorption and load capacity, as shown in Fig. 9. Compared with the axial gradient model, maximum E of the radial gradient structure can be increased by 10.8%, and SEA can be increased by 13.2%. Compared with the uniform model, maximum E of the radial gradient structure can be increased by 6.3%, and SEA can be increased by 7.5%. At the same time, compared with the original model, maximum E of the radial gradient structure is increased by 39.1%, and SEA is increased by 38.7%. Among all structures, PR-opt has the most excellent mechanical properties.

The deformation modes of biomimetic surface structures with the same morphology under quasi-static compression are similar, as shown in Fig. 13. The improved structure deforms more evenly and is less likely to undergo structural failure, but the original structure is prone to suffer from structural failure after compression deformation due to the low curvature of the joints between structural units. The compression deformation mode of the uniform biomimetic surface structure and radial biomimetic surface structure is relatively uniform, with each layer undergoing uniform bending deformation simultaneously. At the same time, it can be observed that the central and lateral regions of the structures exhibit significant deformation in the transverse and loading directions, resulting in a bulging deformation. On the other hand, the axial gradient surface structure undergoes uniform bending deformation layer by layer from top to bottom, corresponding to the step-like rise of the force, as shown in Fig. 10. In terms of stress distribution, the uniform biomimetic surface structure and radial biomimetic surface structure show uniform distribution of overall stress, and the magnitude of the distributed stress is consistent. As shown in Fig. 10, the radial gradient biomimetic surface struc-

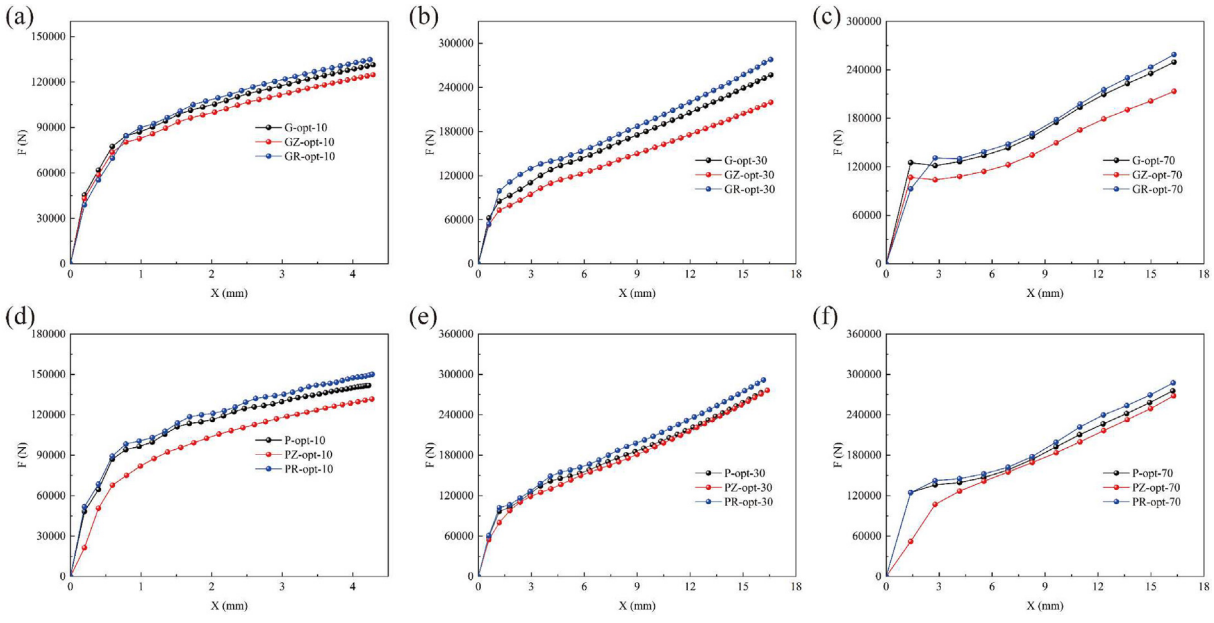

Fig. 14. Structural impact results with initial velocity 10 m/s, 30 m/s, and 70 m/s. (a) Impact force–displacement curve of multimodal biomimetic Gyroid with initial velocity 10 m/s. (b) Impact force–displacement curve of multimodal biomimetic Gyroid with initial velocity 30 m/s. (c) Impact force–displacement curve of multimodal biomimetic Gyroid with initial velocity 70 m/s. (d) Impact force–displacement curve of multimodal biomimetic Primitive with initial velocity 10 m/s. (e) Impact force–displacement curve of multimodal biomimetic Primitive with initial velocity 30 m/s. (f) Impact force–displacement curve of multimodal biomimetic Primitive with initial velocity 70 m/s.

tures have lower stress, indicating that they have better load absorption and dissipation capacity. Meanwhile, the uniform biomimetic surface structures have higher stress and weaker load dissipation capacity. The axial gradient biomimetic surface structures show a gradual decrease in stress distribution from top to bottom. Under the same strain conditions, the part of the axial gradient biomimetic surface structures with low porosity has the lowest stress distribution. This characteristic is of great significance in human protection engineering.

5.4. Crashworthiness characteristics analysis of multimodal biomimetic surface structure

The same numerical model as described in the previous section is used to simulate dynamic impact. A rigid plate with a mass of 10 kg is subjected to free-fall impact with three different initial impact velocities of 10 m/s, 30 m/s, and 70 m/s, respectively. The force–displacement curves obtained from the impact tests are shown in Fig. 14.

The force–displacement curves obtained from impact test have representative regions similar to that of the quasi-static curves. Unlike quasi-static test results, the force–displacement curve under dynamic impact shows an initial peak force, followed by an upward trend.

As the impact velocity increases, the crushing force increases significantly. At the same time, as the impact rate increases, the deviation between peak force and plateau force becomes more and more obvious. This difference is related to the strain rate effect of the structural configuration. It is noted that the yield stress significantly increases with the increase of loading rate. The impact resistance of the structure under three different loading rates shows the following pattern: radial gradient structure > uniform structure > axial gradient structure. By comparing each biomimetic surface structure, it is evident that the radial gradient structure outperforms the uniform structure and the axial gradient structure under dynamic impact, as shown in Fig. 15. Compared with the axial gradient model, maximum E of the radial gradient structure can be increased by 20.6%, and SEA can be increased by 20.8%. At the same time, compared with the uniform model, maximum E of the radial gradient structure can be increased by 7.1%, and SEA can be increased by 7.5%. Among them, PR-opt has the most excellent mechanical properties in resisting impact.

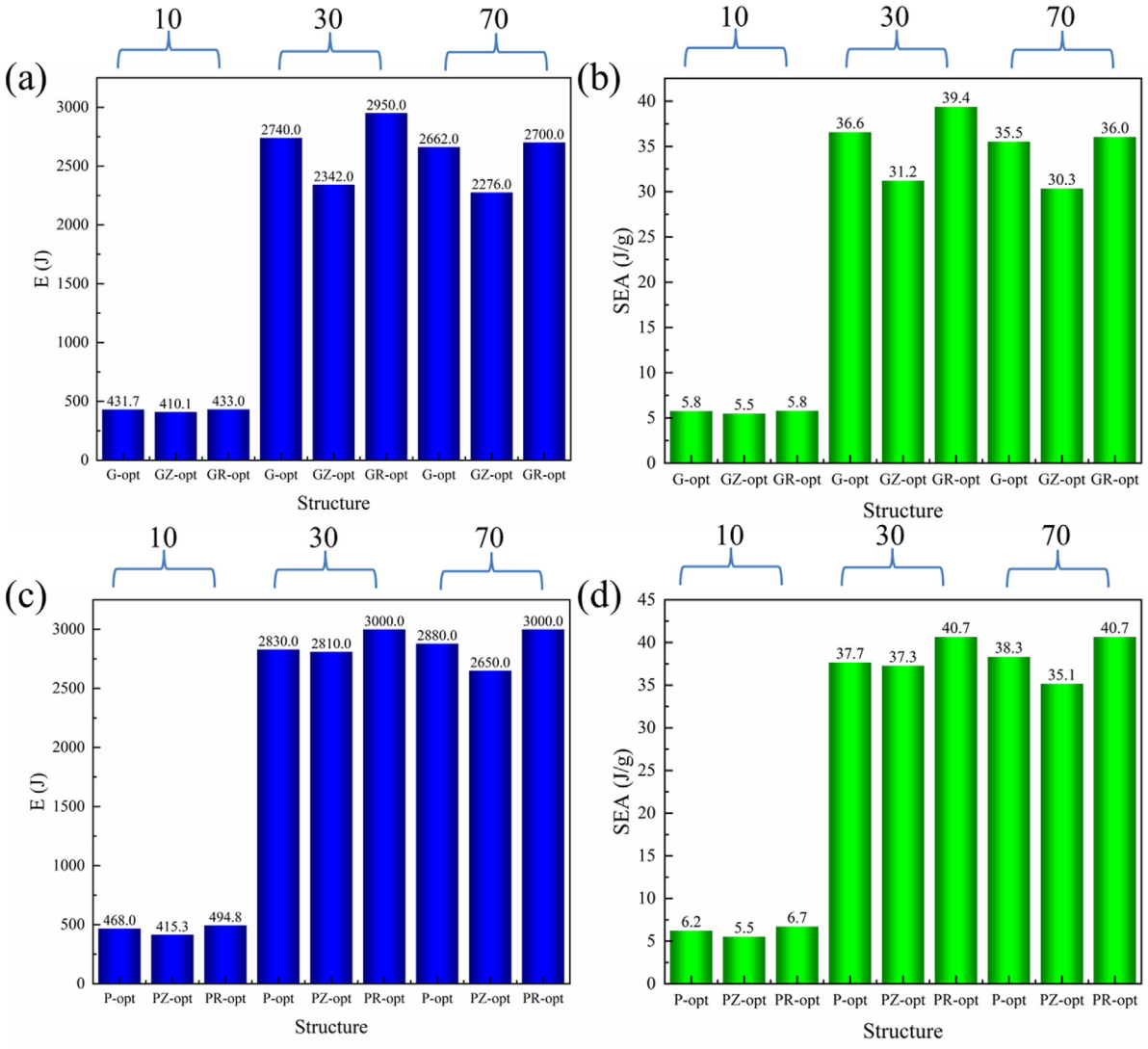

Fig. 15. Structural impact results. (a) E of multimodal biomimetic Gyroid. (b) SEA of multimodal biomimetic Gyroid. (c) E of multimodal biomimetic Primitive. (d) SEA of multimodal biomimetic Primitive.

6. Optimal design of radial gradient surface structure

6.1. Radial parameter transformation of PR-opt

Among the above-mentioned biomimetic multimodal surface structures, PR-opt has the most outstanding mechanical properties. PR-opt is a biomimetic structure that imitates the gradient distribution of femoral density. The porosity in the structural intermediate axis is high, and the porosity gradually decreases along the axis towards the periphery. To investigate PR-opt with the most outstanding performance in radial gradient variation, the porosity gradient center is controlled to move along the y-axis and the diagonal 45° direction, as shown in Fig. 16. The positions of the y-axis and diagonal 45° offset centers are shown in Table 4.

6.2. Crashworthiness analysis of multimodal PR-opt

The numerical model utilized for dynamic impact simulation remains consistent with that outlined in the previous section. A rigid plate weighing 10 kg undergoes free-fall impact at three distinct initial velocities of 10 m/s, 30 m/s, and 70 m/s, are shown in Fig. 17.

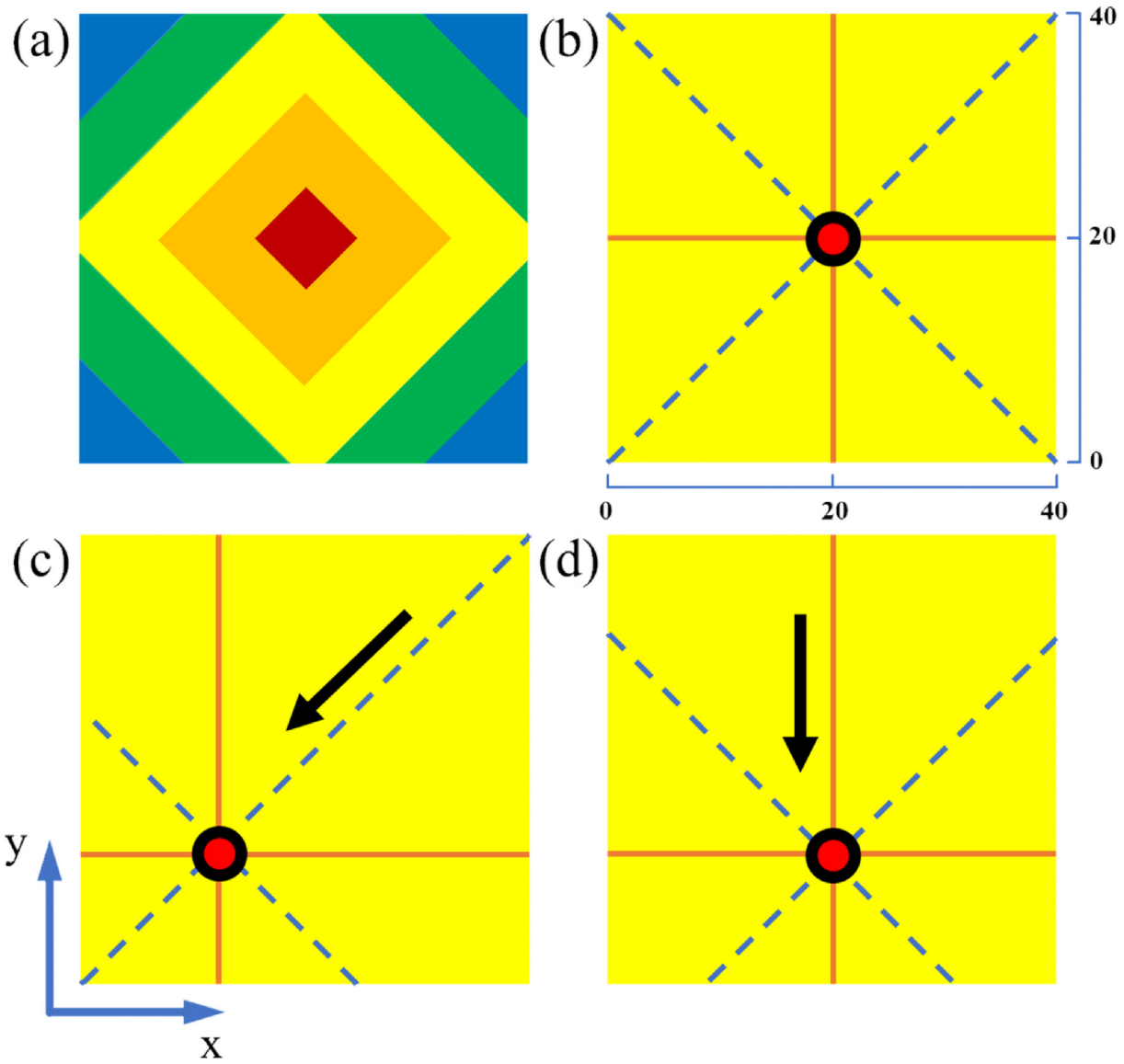

Fig. 16. Radial parameter transformation of PR-opt. (a) Radial gradient distribution. The porosity gradient increases from yellow to blue, and the porosity is from 31.5% to 55.5%. (b) Original radial gradient center. (c) 45° offset radial center. (d) y axial offset radial center. The red dot represents the radial gradient center.

Table 4
Y and oblique 45° offset radial center location.

Structure	0–40		3.5–36.5		7–33		10–30		13.5–26.5		16.5–23.5		20–20	
Coordinate axis	x	y	x	y	x	y	x	y	x	y	x	y	x	y
y shift	20	0	20	3.5	20	7	20	10	20	13.5	20	16.5	20	20
Oblique 45° shift	\	\	\	\	7	7	10	10	13.5	13.5	16.5	16.5	20	20

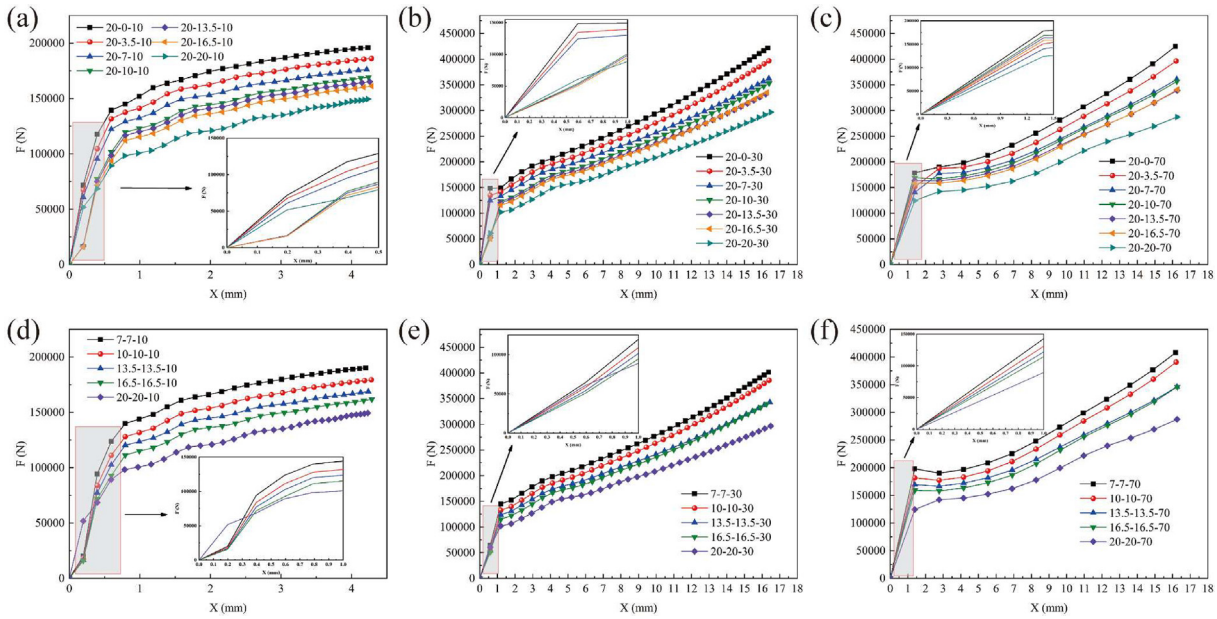

Fig. 17. Impact results of multimodal PR-opt. (a) The force–displacement curve of PR-opt with y center offset at an impact velocity of 10 m/s. (b) The force–displacement curve of PR-opt with y center offset at an impact velocity of 30 m/s. (c) The force–displacement curve of PR-opt with y center offset at an impact velocity of 70 m/s. (d) The force–displacement curve of PR-opt with oblique 45°center offset at an impact velocity of 10 m/s. (e) The force–displacement curve of PR-opt with oblique 45°center offset at an impact velocity of 30 m/s. (f) The force–displacement curve of PR-opt with oblique 45°center offset at an impact velocity of 70 m/s. x-y-v, where x is the x coordinate value, y is the y coordinate value, and v represents the initial impact velocity.

The impact force increases gradually with the increase of impact velocity. However, it is obvious that the bearing capacity of the structure increases gradually with the deviation degree of the radial gradient central, but the uneven distribution of load increases at the same time. This is because one side of the boundary has high porosity, and the diagonal part has lower porosity, which makes the structure have higher resistance to impact in a single direction. When the porosity gradient center of PR-opt is offset, the centers of bending and twisting also offset accordingly. As the deviation degree of the radial gradient central increases, the value p also increases. According to Eq. (23), Eq. (24), and Eq. (28), the bending stress and the twisting stress both increase with the increase of central deviation degree. This is consistent with the simulation results of the structure. But the load direction can come from the side in a real environment, which makes the high porosity parts have very low resistance. Therefore, in practical engineering applications, the structure with a high deviation of the radial gradient center can be used when facing the predictable unidirectional load impact. The structure with the radial gradient center located at the central axis can be adopted when there is uncertain load.

7. Conclusion

This paper studies biomimetic surface structures, which are designed based on the microstructure of biological femurs that are both superb free modes, lightweight, and strong freedom of variable form. The results show that these structures have positive properties, and the following conclusions are drawn:

(1) The concept of large curvature surface factor is introduced to enhance the interfacial fracture behavior of biomimetic surface structures. Novel types of these structures are constructed by combining the large curvature surface factor, resulting in the design of novel radial gradient surface structures and axial gradient surface structures.

(2) Euler theory states that the properties of lattice structures are determined by the relative density of structures. The axial gradient variation of structures can cause them to enter the dense stage earlier, with the high porosity area playing a crucial role in bearing and dissipating energy. The deformation modes of axial gradient structures exhibit layered failure, which is significantly important for targeted applications in protective engineering.

(3) The radial gradient variation of bionic structures enhances their structural durability, resulting in an increase of up to 7.5% compared to other structures. In addition, the load distribution in radially gradient structures is uniform, and the deformation mode exhibits overall failure, which offers better resistance and dissipation of loads. Different radial gradient structures can have diverse engineering applications. As the central axis deviation of radial gradient structures increases, the unidirectional resistance of radial gradient surface structures improves. However, this improvement is accompanied by an increase in the uneven distribution of the load.

Data availability

Data will be made available on request.

Declaration of Competing Interest

The authors declare that they have no known competing financial interests or personal relationships that could have appeared to influence the work reported in this paper.

Acknowledgments

These studies are funded by National Key R&D program of China (2022YFE0138500), the National Natural Science Foundation of China (No. 51975246 and No. 52205310), the Science and Technol-

ogy Development Program of Jilin Province (20220101192JC and 20200404204YY), the Capital construction fund plan within the budget of Jilin Province (No. 2023C041-4) and the Chongqing Natural Science Foundation (No. CSTB2022NSCQ-MSX0225).

Appendix A. Supplementary data

Supplementary data to this article can be found online at https://doi.org/10.1016/j.matdes.2023.112018.

References

[1] L. Auber, The structure producing "non-iridescent" blue colour in bird feathers, J. Zool. 129 (2010) 455–486.
[2] K. Liu, Z.H. Yu, K.Y. Wang, L. Jing, Crashworthiness of bamboo-inspired circular tubes used for the energy absorber of rail vehicles, Acta Mech. Sin. 38 (2022) 122014.
[3] L. Yang, C. Yan, W. Cao, Z. Liu, B.o. Song, S. Wen, C. Zhang, Y. Shi, S. Yang, Compression–compression fatigue behaviour of gyroid-type triply periodic minimal surface porous structures fabricated by selective laser melting, Acta Mater. 181 (2019) 49–66.
[4] K. Chatchai, P. Teerapong, K. Suppakrit, P. Patcharapit, Mechanical and fluid characteristics of triply periodic minimal surface bone scaffolds under various functionally graded strategies, J. Comput. Des. Eng. 9 (2022) 1258–1278.
[5] S. Vijayavenkataraman, Y.K. Lai, F.L. Wen, 3D-printed ceramic triply periodic minimal surface structures for design of functionally graded bone implants, Mater. Des. 191 (2020) 108602.
[6] L.Y. Zhu, L. Li, J.P. Shi, Z.A. Li, J.Q. Yang, Mechanical characterization of 3D printed multi-morphology porous Ti6Al4V scaffolds based on triply periodic minimal surface architectures, Am. J. Transl. Res. 10 (2018) 3443–3454.
[7] L. Zhang, Z.H. Hu, M.Y. Wang, S. Feih, Hierarchical sheet triply periodic minimal surface lattices: design, geometric and mechanical performance, Mater. Des. 209 (2021) 109931.
[8] R. Sankineni, Y. Ravi Kumar, Evaluation of energy absorption capabilities and mechanical properties in FDM printed PLA TPMS structures, Proc. Inst. Mech. Eng. Part C-J. Eng. Mech. Eng. Sci. 236 (7) (2022) 3558–3577.
[9] L.Y. Yang, C.Z. Han, C.J. Chen, P. Yang, S.F. Shi, S.S. Yu, Mechanical response of a triply periodic minimal surface cellular structures manufactured by selective laser melting, Int. J. Mech. Sci. 148 (2018) 149–157.
[10] L. Yang, C. Yan, W. Cao, Z. Liu, B.o. Song, S. Wen, C. Zhang, Y. Shi, S. Yang, C, Compression-compression fatigue behaviour of gyroid-type triply periodic minimal surface porous structures fabricated by selective laser melting, Acta Mater. 181 (2019) 49–66.
[11] D.W. Li, W.H. Liao, N. Dai, G.Y. Dong, Y.L. Tang, Y.M. Xie, Optimal design and modeling of gyroid-based functionally graded cellular structures for additive manufacturing, Comput.-Aided Des. 104 (2018) 87–99.
[12] A. Ronca, G. Rollo, P. Cerruti, G.X. Fei, X.P. Gan, G.G. Buonocore, M. Lavorgna, H. S. Xia, C. Silvestre, L. Ambrosio, Selective laser sintering fabricated thermoplastic polyurethane/ graphene cellular structures with tailorable properties and high strain sensitivity, Appl. Sci. 9 (2019) 864.
[13] L. Yang, C.Z. Yan, H.Y. Fan, Z.Q. Li, C. Cai, P. Chen, Y.S. Shi, S.F. Yang, Investigation on the orientation dependence of elastic response in Gyroid cellular structures, J. Mech. Behav. Biomed. Mater. 90 (2019) 73–85.
[14] C. Zhang, H. Zheng, L. Yang, Y. Li, J.L. Jin, W.C. Cao, C.Z. Yan, Y.S. Shi, Mechanical responses of sheet-based gyroid-type triply periodic minimal surface lattice structures fabricated using selective laser melting, Mater. Des. 214 (2022) 110407.
[15] M. Zhao, D.Z. Zhang, F. Liu, Z.H. Li, Z.B. Ma, Z.H. Ren, Mechanical and energy absorption characteristics of additively manufactured functionally graded sheet lattice structures with minimal surfaces, Int. J. Mech. Sci. 167 (2020) 105262.
[16] D.S.J. Al-Saedi, S.H. Masood, F.U.R. Muhammad, A. Alomarah, P. Ponnusamy, Mechanical properties and energy absorption capability of functionally graded F2BCC lattice fabricated by SLM, Mater. Des. 144 (2018) 32–44.
[17] A. Kostadinov, L. Yan, A. Teo, G. O'Neill, Slanted and cluttered: Solving deficiencies in SLM-manufactured lattice geometries, Mater. Des. 211 (2021) 110130.
[18] T. Poltue, C. Karuna, S. Khrueaduangkham, S. Seehanam, P. Promoppatum, Design exploration of 3D-printed triply periodic minimal surface scaffolds for bone implants, Int. J. Mech. Sci. 211 (2021) 106762.
[19] C. Yan, L. Hao, A. Hussein, P. Young, Ti-6Al-4V triply periodic minimal surface structures for bone implants fabricated via selective laser melting, J. Mech. Behav. Biomed. Mater. 51 (2015) 61–73.
[20] Q.D. Sun, J. Sun, K. Guo, L.S. Wang, Compressive mechanical properties and energy absorption characteristics of SLM fabricated Ti6Al4V triply periodic minimal surface cellular structures, Mech. Mater. 166 (2022) 104241.
[21] M. Vaezi, H. Seitz, S. Yang, A review on 3D micro-additive manufacturing technologies, Int. J. Adv. Manuf. Technol. 67 (2013). 1957–1957.
[22] Y. Tripathi, M. Shukla, A.D. Bhatt, Implicit-function-based design and additive manufacturing of triply periodic minimal surfaces scaffolds for bone tissue engineering, J. Mater. Eng. Perform. 28 (12) (2019) 7445–7451.
[23] N. Yang, Y. Tian, D. Zhang, Novel real function based method to construct heterogeneous porous scaffolds and additive manufacturing for use in medical engineering, Med. Eng. Phys. 37 (11) (2015) 1037–1046.
[24] C.N. Kelly, A.S. Lin, K.E. Leguineche, S. Shekhar, W.R. Walsh, R.E. Guldberg, K. Gall, Functional repair of critically sized femoral defects treated with bioinspired titanium gyroid-sheet scaffolds, J. Mech. Behav. Biomed. Mater. 116 (2021) 104380.
[25] D.W. Li, W.H. Liao, N. Dai, Y.M. Xie, Comparison of mechanical properties and energy absorption of sheet-based and strut-based gyroid cellular structures with graded densities, Materials 12 (2019) 2183.
[26] X.F. Cao, H.M. Yang, X.B. Ren, W.W. Wu, L. Xi, Y. Li, D.N. Fang, Mechanical performance and defect analysis of the imperfect micro smooth gyroid cylinder shell structure, Compos. Struct. 273 (2021) 114320.
[27] M.K. Zhang, Y.Q. Yang, W.T. Qin, S.B. Wu, J. Chen, C.H. Song, Optimizing the pinch-off problem for gradient triply periodic minimal surface cellular structures manufactured by selective laser melting, Rapid Prototyping J. 26 (2020) 1771–1781.
[28] W.M. Jiang, W.H. Liao, T.T. Liu, X. Shi, C. Wang, J.F. Qi, Y. Chen, Z. Wang, C.D. Zhang, A voxel-based method of multiscale mechanical property optimization for the design of graded TPMS structures, Mater. Des. 204 (2021) 109655.
[29] D.-J. Yoo, Advanced porous scaffold design using multi-void triply periodic minimal surface models with high surface area to volume ratios, Int. J. Precis. Eng. Manuf. 15 (8) (2014) 1657–1666.
[30] R.Y. Liu, G.F. Yao, K.Y. Gao, Z.Z. Xu, Y.N. Yang, X. Guo, Z.L. Yu, Z.H. Zhang, C.Y. Han, Study on mechanical properties of lattice structures strengthened by synergistic hierarchical arrangement, Compos. Struct. 304 (2023) 116304.
[31] A. Chinsamy, J.H.H. Chinsamy, A.A. Hurum, Bone microstructure and growth patterns of early mammals, Acta Palaeontol. Pol. 51 (2006) 325–338.
[32] R. Dai, Y. Ma, Z. Sheng, Y. Jin, Y. Zhang, L. Fang, H. Fan, E. Liao, Effects of genistein on vertebral trabecular bone microstructure, bone mineral density, microcracks, osteocyte density, and bone strength in ovariectomized rats, J. Bone Miner. Metab. 26 (4) (2008) 342–349.
[33] C.Z. Yan, L. Hao, A. Hussein, Q.S. Wei, Y.S. Shi, Microstructural and surface modifications and hydroxyapatite coating of Ti-6Al-4V triply periodic minimal surface lattices fabricated by selective laser melting, Mater. Sci. Eng. C-Mater. Biol. Appl. 75 (2017) 1515–1524.
[34] X.H. Wang, J.Y.H. Fuh, Y.S. Wong, Y.X. Tang, Laser sintering of silica sand-mechanism and application to sand casting mould, Int. J. Adv. Manuf. Technol. 21 (12) (2003) 1015–1020.
[35] J.-Y. Liu, H.-T. Liu, M.-R. An, Crushing behaviors of novel Diabolo shaped honeycombs with enhanced energy absorption performance, Int. J. Mech. Sci. 229 (2022) 107492.
[36] C. Yan, L. Hao, A. Hussein, P. Young, J. Huang, W. Zhu, Microstructure and mechanical properties of aluminium alloy cellular lattice structures manufactured by direct metal laser sintering, Mater. Sci. Eng. A-Struct. Mater. Prop. Microstruct. Process. 628 (2015) 238–246.
[37] K.S. Lee, S.K. Kim, I.Y. Yang, The energy absorption control characteristics of Al thin-walled tube under quasi-static axial compression, J. Mater. Process. Technol. 201 (1-3) (2008) 445–449.
[38] J.Q. Qi, C. Li, Y. Tie, Y.P. Zheng, Y.C. Duan, Energy absorption characteristics of origami-inspired honeycomb sandwich structures under low-velocity impact loading, Mater. Des. 207 (2021) 109837.
[39] L.J. Gibson, Cellular solids, MRS Bull. 28 (4) (2003) 270–274.
[40] N.A.Z. Abdullah, M.S.M. Sani, M.S. Salwani, N.A. Husain, A review on crashworthiness studies of crash box structure, Thin-Walled Struct. 153 (2020) 106795.
[41] M.Y. Zhang, Q. Yu, Z.Q. Liu, J. Zhang, G.Q. Tan, D. Jiao, W.J. Zhu, S.J. Li, Z.F. Zhang, R. Yang, R.O. Ritchie, 3D printed Mg-NiTi interpenetrating-phase composites with high strength, damping capacity, and energy absorption efficiency, Sci. Adv. 6 (2020) eaba5581.